TIDAL CONSTRAINTS ON THE MARTIAN INTERIOR. L. Pou[1], F. Nimmo[1], A. Rivoldini[2], A. Khan[3,4], A. Bagheri[3], T. Gray[3], H. Samuel[5], P. Lognonné[5], A.-C. Plesa[6], T. Gudkova[7], D. Giardini[3] [1]University of California Santa Cruz, Dept. Earth and Planetary Sciences, 1158 High Street, CA 95064, United States (lpou@ucsc.edu) [2]Royal Observatory of Belgium, Avenue Circulaire 3, B-1180 Brussels, Belgium [3]Institute of Geophysics, ETH Zürich, Sonneggstrasse 5, 8092 Zürich, Switzerland [4]Physik-Institut, University of Zurich, Zurich, Switzerland [5]Institut de Physique du Globe de Paris, Université Paris Diderot-Sorbonne Paris Cité, 35 rue Hélène Brion - Case 7071, Lamarck A, 75205 Paris Cedex 13, France [6]Planetary Physics, Institute of Planetary Research, German Aerospace Center (DLR), Rutherfordstraße 2, Berlin 12489, Germany [7]Schmidt Institute of Physics of the Earth, Russian Academy of Sciences, Moscow 123242, Russia

Introduction: The study of the tidal response of Mars provides insights into the interior properties of the planet, and especially its deep structure [1,2]. In this work, we match existing interior models of Mars to the most recent observations of the tidal response of Mars. We produce a comparative study of the obtained models and evaluate how the interior and dissipation of Mars are impacted by the tidal constraints provided by the Love number k_2 and the secular acceleration in longitude s of its main moon, Phobos.

Tidal constraints: The tidal forcing from Phobos distorts the shape of Mars into a tidal bulge and creates displacements, changes in gravitational potential, and variations of surface gravity. The changes in the gravitational potential can be measured by tracking the position of an orbiter to constrain the Love number k_2^s of Mars for the degree-2 Solar tide [3].

Anelastic dissipation in the Martian interior causes the tidal bulge of Mars to be misaligned with Phobos by the geometric lag angle [4]. This angle depends on the internal dissipation in Mars and creates a braking effect on the Martian moon from which the secular acceleration of Phobos can be obtained [5]. The values used for this study are given in Table 1.

Tidal parameter	Values	Source
Love number k_2^s of Mars	0.174 ± 0.08	[5]
Secular acceleration s of Phobos (mdeg.yr^{-2})	1.273 ± 0.003	[5]

Table 1: Tidal constraints to be satisfied by all models.

Derivation of the secular acceleration of Phobos: Because of the proximity of Phobos to Mars, higher-degree tides must be considered in the calculation of the secular acceleration s. Based on the works of [6], given the negligible inclination and eccentricity of Phobos and our focus on the equatorial tidal bulge of Mars, the expression for the secular acceleration is (1):

$$s = \frac{3}{2}\frac{m^*}{m}n^2\left[\frac{3}{2}\frac{k_{2200}}{Q_{2200}}\left(\frac{r}{a^*}\right)^5 + \frac{3}{8}\left(\frac{k_{3110}}{Q_{3110}} + 5\frac{k_{3300}}{Q_{3300}}\right)\left(\frac{r}{a^*}\right)^7 + \frac{5}{16}\left(2\frac{k_{4210}}{Q_{4210}} + 7\frac{k_{4400}}{Q_{4400}}\right)\left(\frac{r}{a^*}\right)^9 + \frac{15}{128}\left(2\frac{k_{5120}}{Q_{5120}} + 7\frac{k_{5310}}{Q_{5310}} + 21\frac{k_{5500}}{Q_{5500}}\right)\left(\frac{r}{a^*}\right)^{11}\right]$$

where m^* and m are the mass of Phobos and Mars, respectively, r is the radius of Mars, a^* is the semimajor axis of Phobos, and k_{lmpq} and Q_{lmpq} are the Love number and the tidal quality factor for the Phobos tide of degree l and order m, respectively. The Love numbers and tidal quality factor are frequency dependent and must be calculated for $T_{lm} = T_1/m$ where T_1 = 11h 06min is the synodic period of Phobos.

Martian models: We study 5 families of models: the FN models based on [7], the AB models based on [8,9], the HS models based on [10], the TG models based on [11], and the AR models based on [12-15]. Except for the AB models constructed by inverting geophysical parameters to match the data, we adjust several parameters (core size, temperature…) to match Table 1. Core size estimates are summarized in Fig. 1.

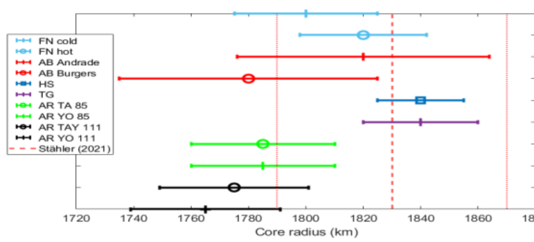

Figure 1: Core ranges for each of our models matching the parameters in Table 1. Most models show good compatibility with seismic observations of the Martian core in [16], except the AR and AB Burgers models where only the largest core sizes match them.

Temperature and lithosphere thickness: We compare our temperature profiles with estimations of the lithosphere thickness. To fit the elastic thickness of the lithosphere T_e at the poles from [17-18], an average T_e of 275±10 km is needed, corresponding to the green box in Fig. 2. This is compatible with seismic observations of the upper mantle in [19] and geotherms in [20] and favor models assuming colder mantle temperatures.

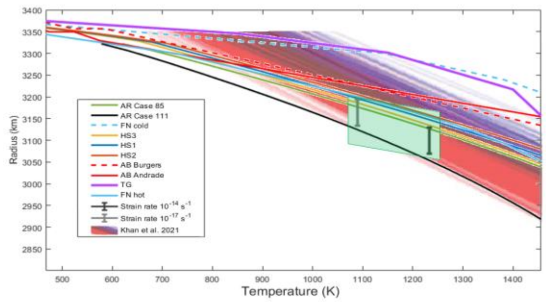

Figure 2: Temperature profiles for our models, compared to the inverted geotherms from [19] and the elastic thickness of the lithosphere estimations from [17-18] represented by the green box. Colder mantle temperatures are favored.

Synergy with seismic measurements: From the measurements of k_2^s and s, the tidal bulk attenuation of Mars Q_{2200} is strongly constrained with Eq. (1) at the frequencies of the Phobos tides (between 11.1hr and 2.2hr). However, due to the different rheology models and temperature profiles, the models yield distinct Q_μ profiles at seismic frequencies, as illustrated in Fig. 3. Measurements of the seismic shear attenuation in the deepest part of the mantle with an accuracy better than ± 500 would be able to distinguish between models.

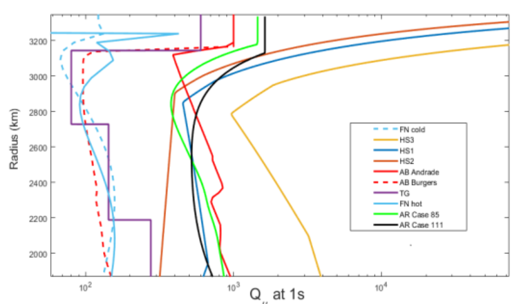

Figure 3: Shear attenuation Q_μ profiles at 1s for our models. An accuracy better than ± 500 on the attenuation in the lower mantle of Mars would be sufficient to distinguish between our models.

Chandler Wobble: Predictions of the Chandler Wobble period are shown in Fig. 4 for our models, compared to the measurements from [3]. While all our models match k_2^s for the Solar tide, they do not match P_{CW} at 206.9 days. However, while P_{CW} is sensitive to the frequency dependency α of Q_μ, there are also other influences at play. Fig. 4 therefore only indicates likely values rather than a direct determination of α.

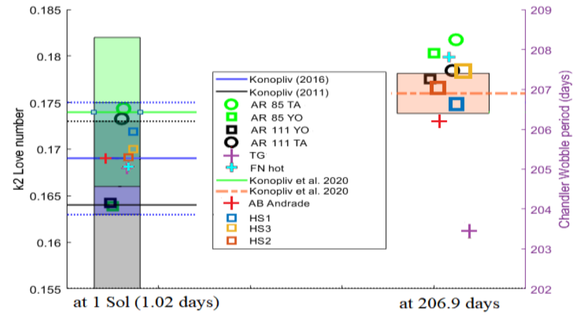

Figure 4: Comparison of the k_2^s and P_{CW} values (left and right, respectively) for our models. Left areas are based on Table 1, while the right orange area is from the P_{CW} estimation of [3].

Acknowledgments: Numerical computations were partly performed on the S-CAPAD platform, IPGP, France. T. Gudkova thanks a government contract of the Schmidt Institute of Physics of the Earth of the Russian Academy of Sciences. A. Bagheri was supported by a grant from the Swiss National Science Foundation (project 172508). This work is supported in part by the NASA InSight participating scientist program (NNH17ZDA001N-INSTPSP).

References: [1] Lognonné P. and Mosser B (1993) Surv. Geophys. 14, 239-302. [2] Van Hoolst T. et al. (2003) Icarus 161(2), 281-296. [3] Konopliv A. S. et al. (2020) Geophys. Res. Lett., 47(21). [4] MacDonald G. J. F. (1964) Science 145(3635), 881-890. [5] Jacobson R. A. and Lainey V. (2014) Planet Space Sci 102, 35-44. [6] Kaula W. M. (1964) Rev. Geophys. 2(4), 661-685. [7] Nimmo F. and Faul U. H. (2013) J. Geophys. Res. Planets 118(12), 2558-2569. [8] Khan A. et al. (2018) J. Geophys. Res. Planets 123(2), 575-611. [9] Bagheri A. et al. (2019) J. Geophys. Res. Planets 124(11), 2703-2727. [11] Samuel H. et al. (2021) J. Geophys. Res. Planets 1-61. [12] Zharkov V. N. et al. (2017) Sol. Syst. Res. 51(6), 479-490. [14] Rivoldini A. et al. (2011) Icarus 213(2), 451. [13] Plesa A.-C. et al. (2018) Geophys. Res. Lett. 45(22), 12,198-12,209. [14] Taylor G. J. (2013) Chem. Erde. 73(4), 401-420. [15] Yoshizaki T. and McDonough W. F. (2018) Geochim. Cosmochim. Acta 273, 137-162. [16] Stahler S. C. et al. (2021) Science 373(6553), 433-448. [17] Broquet A. et al. (2020) Geophys. Res. Lett. 47(5). [18] Broquet A. et al. (2021) J. Geophys. Res. Planets 126(8). [19] Khan et al. (2021) Science 373(6553), 434-438. [20] Khan et al. (2022) Earth Planet. Sci. Lett. 578, 117330.